Numerical Computation Of Multi-Component Two-Phase Flow in Cathode Of PEM Fuel Cells

M. Khakbaz Baboli[i] and M. J. Kermani[ii] *

Received 28 November 2007; received in revised 24 August 2010; accepted 8 May 2011

ABSTRACT

A two-dimensional, unsteady, isothermal and two-phase flow of reactant-product mixture in the air-side electrode of proton exchange membrane fuel cells (PEMFC) is studied numerically in the present study. The mixture is composed of oxygen, nitrogen, liquid water and water vapor. The governing equations are two species conservation, a single momentum equation for mobile mixture, liquid mass conservation, and the whole mixture mass conservation. In this study, liquid mass conservation is used to calculate the saturation, so, the effect of liquid phase velocity and also saturation at previous time step are accounted in calculating the next time step saturation. The capillary pressure was used to express the slip velocity between the phases. The strongly coupled equations are solved using the finite volume SIMPLER scheme of Patankar (1984). The computational domain consists of an open area (gas delivery channel), and a porous Gas Diffusion Layer (GDL). A single set of governing equations are solved for both sub domains with respect to each sub domain property. The comparison between the numerical current density and that of experimental (Ticianelli et al.(1988)) shows a good agreement.

KEYWORDS

CFD, PEM Fuel Cells, Two-Phase, Two Component.

1. INTRODUCTION

Two-phase modeling of PEM fuel cells is necessary due to the strong effect of liquid water existence in porous cathode GDL on fuel cell performance. The prediction of the phenomena happening as liquid water forms, is a contribution to optimization of water management and fuel cell design. Water is generated at the cathode-membrane interface due to the electrochemical reaction and phase change may occur as a result of the increase in water vapor partial pressure beyond the saturation pressure at mixture temperature. If the excessive generated water is not removed from the cathode, flooding may occur and liquid water will fill the pores partially acting like solid matrix, so, the oxygen transport to the catalyst layer is hindered. There have been some studies on the water generation and its transport as well as performance modeling for PEM fuel cells. Bernardi and Verbrugge [3],[4] and Springer[5] performed one-dimensional models, that were a start point in PEM fuel cells modeling.

One-dimensional models are unable to simulate the components and phase distribution along the channel. The two-dimensional models by Fuller and Newman and Nguyen and White [6] assumed that diffusion was the only mechanism for oxygen transport and did not consider the interaction of the flow with the species field in the channel and gas diffuser. Gurau and Liu [7] modeled the coupled flow and transport equations in the flow channel and the gas diffuser in a single-phase and incompressible form. Z.H. Wang, C.Y. Wang and K.S. Chen [8] and also Lixin You and Hongtan Liu [10] have performed a steady numerical study considering the difference in phase velocities, but in their model the diffusion coefficients were constant and the saturation was not affected by liquid velocity. Dilip Natarajan and Trung Van Nguyen [9] just

[i] Graduate Student, member of Energy Conversion Research Laboratory, Department of Mechanical Engineering Amirkabir University of Technology (Tehran Polytechnic) Tehran, Iran, 15875—4413, mobinkhakbaz@gmail.com.

[ii] * Corresponding Author, Associate Professor of Mechanical Engineering, Department of Mechanical Engineering, Also with Renewable Energy Research Center (Fuel Cell Group), Amirkabir University of Technology (Tehran Polytechnic), Tehran, Iran, 15875—4413, mkermani@aut.ac.ir

modeled a transversal cross section of the fuel cell and did not account the effect of inlet velocity in gas channel on the flow field and species transport. In this paper, a two-dimensional, unsteady, isothermal and two-phase flow of reactant-product gases in the air-cathode of (PEMFC) is studied numerically. The model geometry is shown in Fig. 1. The mixture is composed of oxygen, nitrogen, water vapor and liquid water in which the slip velocity between the phases are included.

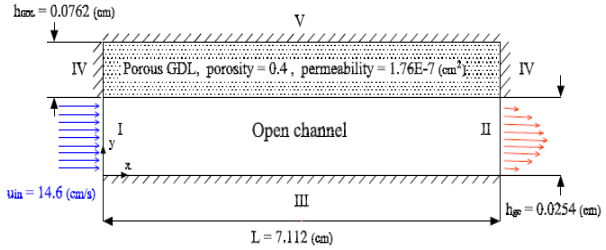

Figure 1. Schematic figure of the computational domain including the dimensions. The GDL porosity and permeability are taken: ε=0.4 and K=1.76 10^{-7} cm^2.

2. GOVERNING EQUATIONS

The governing equations of the fluid motion used in the present multi-component and two-phase flow are given as follows:

The continuity of the two-phase mixture (gas + liquid) [14]:

$$\frac{\partial(\varepsilon\rho)}{\partial t}+\nabla.(\varepsilon\rho\vec{V})=0 \qquad (1)$$

where ε is porosity of the GDL taken as constant, ρ and $\vec{V}$ are the density and the mass averaged velocity of the two-phase mixture, respectively.

The continuity equation for the liquid phase (just water) [14]:

$$\frac{\partial(\varepsilon\rho)}{\partial t}+\nabla.(\varepsilon s\,\rho_l\vec{V}_l)=\dot{S}_l, \qquad (2)$$

where ρ_l liquid density taken as a constant ρ_l=998 kg/m^3, s is the saturation, $\dot{S}_l$ is the condensation rate (the source term), and $\vec{V}_l$ is the liquid water velocity to be determined from Eqn. 10. The source term is obtained as follows [14]:

$$\dot{S}_l=-\frac{1}{\Delta t}\left[P_{sat}\left(\frac{(1-s)}{R_{H_2O}}\right)^{t+\Delta t}-P_{H_2O}\left(\frac{(1-s)}{R_{H_2O}}\right)^{t}\right], \qquad (3)$$

from which P_{H_2O} and P_{sat} are the partial pressure of water vapor at next time step, the only difference is that P_{H_2O} is thermodynamically unstable but P_{sat} is stable. P_{sat} is the saturation pressure obtained at the mixture temperature from [8]:

$$\log_{10}P_{sat}=-2.1794+0.02953tt-9.1837\times10^{-5}tt^2+1.4454\times10^{-7}tt^3, \qquad (4)$$

where tt = T-273.15, P_{sat} is obtained in atmosphere. It is noted that $\dot{S}_l$ is set equal to zero within the open channel as recommended in [9].

The concentration equation for the water vapor [14]:

$$\frac{\partial\left(\varepsilon(1-s)\rho_g C_g^{H_2O}\right)}{\partial t}+\nabla.\left(\varepsilon(1-s)\vec{N}_{H_2O}\right)=\dot{S}_g, \qquad (5)$$

where P_g is gas phase density and $\vec{N}_{H_2O}$ is the mass flux of water vapor as:

$\vec{N}_{H_2O}=\rho_{H_2O}\vec{V}_g+\vec{J}_{H_2O}$ where $\vec{J}_{H_2O}$ is the diffusive flux of water vapor is obtained from the Maxwell-Stefan equation [1], and $C_g^{H_2O}$ is the mass fraction of water vapor as: $C_g^{H_2O}=\rho_g^{H_2O}/\rho_g$. In Eqn. 5, $\dot{S}_g$ is the evaporation rate of water determined by: $\dot{S}_g=-\dot{S}_l$, and $\vec{V}_g$ is the gas phase mass averaged velocity to be determined from Eqn. 10.

The concentration equation for oxygen [14]:

$$\frac{\partial\left(\varepsilon(1-s)\rho_g C_g^{O_2}\right)}{\partial t}+\nabla.\left(\varepsilon(1-s)\vec{N}_{O_2}\right)=0, \qquad (6)$$

where $\vec{N}_{O_2}$ is the mass flux of oxygen component as: $\vec{N}_{O_2}=\rho_{O_2}\vec{V}_g+\vec{J}_{O_2}$, where $\vec{J}_{O_2}$ is the diffusion of O_2 obtained from the Maxwell-Stefan equation, and $C_g^{O_2}$ is the mass fraction of the oxygen component as: $C_g^{O_2}=\rho_g^{O_2}/\rho_g$.

The Maxwell-Stefan equation for molar diffusive flux of any component in a mixture with more than two components is as follows:

$$\nabla Y_i=\sum\frac{1}{nD_{ij}^e}\left(Y_iJ_j^*-Y_jJ_i^*\right), \qquad (7)$$

where Y_i is the mole fraction of component i, n is the molar gas density, D_{ij}^e is the effective binary diffusion coefficient, and J_i^* is the molar diffusion of component i. D_{ij}^e is the effective diffusion coefficient given by Bruggemann equation [13]:

$$D_{ij}^e=D_{ij}\left(\varepsilon(1-s)\right)^{1.5}, \qquad (8)$$

Note that $J_i\ (kg/sm^2)$ is obtained from $J_i^*(kg/sm^2)$.

Momentum equation for the two-phase mixture in open channel and the porous GDL are presented in a unified form as given below. The unified form is useful as it needs no boundary condition at the channel-GDL interface [14].

$$\frac{\partial\left(\varepsilon\rho\vec{V}\right)}{\partial t}+\nabla.(\varepsilon\rho\vec{V}\vec{V})=-\varepsilon\nabla P+\nabla.(\varepsilon\mu\nabla\vec{V})+\varepsilon\rho_k\vec{g}-\frac{\varepsilon^2\mu}{K}\vec{V}, \quad (9)$$

where ρ is the two-phase mixture density obtained from Eqn. 15 and μ is its viscosity given by Eqn. 17, ρ_k is the kinetic density obtained from Eqn. 16.

The phase velocity components are obtained as follows [14]:

$$\varepsilon\rho_l\vec{V}_l=\vec{J}_l+\varepsilon\lambda_l\rho\vec{V},\ \varepsilon\rho_g\vec{V}_g=\vec{J}_g+\varepsilon\lambda_g\rho\vec{V} \quad (10)$$

where $\vec{J}$ is the phase diffusion encompassing the difference between liquid or gas phase momentum and the mixture momentum ($\vec{J}_g=-\vec{J}_l$)[14]:

$$\vec{J}_l=\frac{\lambda_l\lambda_g K}{\nu}\left[\nabla P_c+\left(\rho_l-\rho_g\right)\vec{g}\right], \quad (11)$$

where ν is the mixture kinematic viscosity (=μ/ρ), and λ is the relative mobility, with the value for liquid and gas phases obtained from [14]:

$$\lambda_l=\frac{k_{rl}/\nu_l}{k_{rg}/\nu_g+k_{rl}/\nu_l},\ \lambda_g=1-\lambda_l, \quad (12)$$

where K_{rl} and K_{rg} are relative permeabilities of liquid and gas obtained from Eqn. 18. ν_l and ν_g are kinematic viscosity of liquid and gas respectively. P_c in Eqn. 11 is the capillary pressure for hydrophilic surfaces determined from [8]:

$$P_c=C\left[1.417(1-s)-2.120(1-s)^2+1.263(1-s)^3\right], \quad (13)$$

where $C=\sigma_c\cos\theta_c\left(\varepsilon/K\right)^{1/2}$, in which σ_c and θ_c are the surface tension and

contact angle, respectively, taken as constants: σ_c = 0.0625 N/m, and θ_c=0 for the hydrophilic surface in the present study.

The ideal gas law is used for the gas density:

$$\rho_g=\frac{P}{R_gT},\ R_g=\bar{R}/M_g, \quad (14)$$

where R_g and M_g are the gas constant and its molecular weight, respectively, and $\bar{R}$ is the universal gas constant.

Density of the total mixture (including both phases) is obtained from [14]:

$$\rho=(1-s)\rho_g+s\rho_l. \quad (15)$$

The kinetic density ρ_k appeared in the momentum equation (Eqn. 9) is included to account for the response of each of the phase on gravitational acceleration $\vec{g}$ [14]:

$$\rho_k=\rho_g\lambda_g+\rho_l\lambda_l. \quad (16)$$

The parameter ρ_k reduces to its limiting value of ρ_k or ρ_l when s=0 and s=1, respectively. The two-phase mixture viscosity is obtained from [14]:

$$\mu=\frac{\rho_l s+\rho_g(1-s)}{k_{rg}/\nu_g+k_{rl}/\nu_l}. \quad (17)$$

It is noted that μ reduces to its limiting value of μ_g or μ_l when s=0 and s=1, respectively. The relative permeability for the phases are [8]:

$$K_{rl}=s^3\ and\ K_{rg}=(1-s)^3. \quad (18)$$

These parameters are dimensionless correction coefficients multiplied by the intrinsic permeability of the porous GDL (*K*) to obtain each phase permeability.

3. SOLUTION PROCEDURE

The set of equations explained in Sec. contains six unknowns as mixture pressure the saturation water vapor and oxygen concentrations, the mixture velocity components, and the (see Eqns. 1, 2, 5, 6, 9). Other parameters just introduce new variables and can be evaluated in terms of these six variables. The PDE's are discretized using the power law method, A code was developed for the unsteady solution of this set of PDE's using the SIMPLER scheme of Patankar (1984). The grid network used for numerical modeling is shown in Fig. 2. The grid network consists of two fine and coarse portions, the former covers the porous GDL and overlaps gas channel partially in order to catch strong gradient around gas channel-GDL interface and the latter covers the rest of gas channel (gas channel-GDL interface is over the two grid networks interface).

4. BOUNDARY CONDITIONS

The boundary conditions, applied to the computational domain shown in Fig. 1, are described as follows.

At boundary location *I* (channel inlet), uniform velocity and mass fraction of species H_2O and O_2 were specified, i.e.:

$$u=u_{in},v=0,C_g^{H_2O}=C_{g\,in}^{H_2O},C_g^{O_2}=C_{g\,in}^{O_2}. \quad (19)$$

where u_{in} is the x-component of velocity at the channel inlet, and $C_{g\,in}^{H_2O}$ and $C_{g\,in}^{O_2}$ refer to the mass fraction of H_2O and O_2 at the channel inlet.

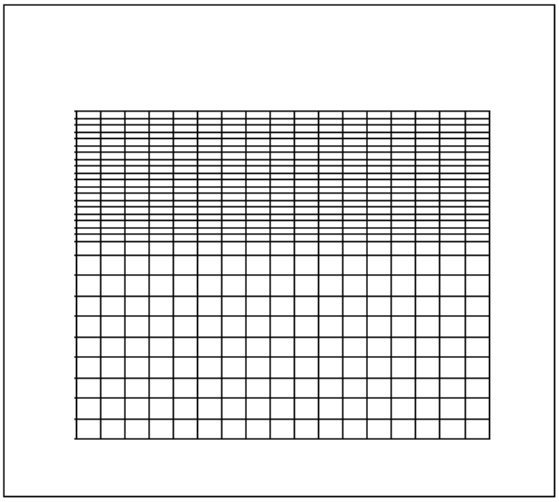

Figure 2. A portion of coarse grid configuration used in computation.

The inlet velocity u_{in} was not explicitly specified in Ticianelli et al. [2]. However, to estimate a reasonable value for u_{in} (or correspondingly the mass flow at the channel inlet, $\dot{m}_{in}=[kg/s]$) the highest current density of the cell (I_{max}) with a stoichiometry coefficient are assumed. According to Ticianelli et al. [2] I_{max} = 2087.74 mA/cm^2, which corresponds to an overpotential of η=0.835*V*. The procedures of the evaluation of $\dot{m}_{in}$ and u_{in} are explained as follows:

The supplied air flow to the channel ($\dot{m}_{in}$) should include, at least, oxygen mass flow rate that is obtained according to the Faraday law $\left(\dot{m}_{O_2}\right)_{consumed}=M_{O_2}I_{\max}.(A_{cl}/2F)$, where A_{cl} is the GDL/catalyst layer interface area (note that current density on polarization curve is reported based on A_{cl} , so, its dimension is A/cm^2). But if the supplied oxygen at the inlet to the channel is limited by $\left(\dot{m}_{O_2}\right)_{consumed}$ then the oxygen flow rate at the exit would be zero. This is a practically impossible operating condition for the cell. Moreover, regardless of its practicality it will give a zero local current density at the exit of the channel, which is not efficient. To be realistic and avoid the deficiency a stoichiometry coefficient $\zeta=3$ is used in the present study [12], $\dot{m}_{O_2}=\zeta.\dot{m}_{O_2\,consumed}$. Therefore, the mass flux of dry air at the inlet to the channel would be $(\dot{m}_{in})_{dry}=\dot{m}_{O_2}+\dot{m}_{N_2}$. Noting that:

$$\frac{\dot{m}_{N_2}}{\dot{m}_{O_2}}=\frac{Y_{N_2}}{Y_{O_2}}\frac{M_{N_2}}{M_{O_2}}, \tag{20}$$

where $Y_{N_2}/Y_{O_2}=79/21$, $M_{O_2}=32\,kg/kmol$, and $M_{N_2}=28\,kg/kmol$. Then, the ratio of mass fluxes of nitrogen to the oxygen at the inlet to the channel would be: $\dot{m}_{N_2}/\dot{m}_{O_2}=3.2917$. Hence, the mass flux for the dry air at the inlet can be obtained in terms of current density as:

$$(\dot{m}_{in})_{dry}=\dot{m}_{O_2}\left(1+\frac{\dot{m}_{N_2}}{\dot{m}_{O_2}}\right)=4.291\zeta\frac{M_{O_2}I}{2F}. \tag{21}$$

For the moisten air entering the channel, one can write:

$$\dot{m}_{in}=(\dot{m}_{in})_{dry}+\dot{m}_v, \tag{22}$$

where $\dot{m}_v$ is the vapor mass flux at the channel inlet. $\dot{m}_v$ is determined using the humidity ratio ω, also known as specific humidity,

$$\omega=\frac{\dot{m}_v}{(\dot{m}_{in})_{dry}}=\frac{M_vP_v}{M_{dry-air}P_{dry-air}}=\frac{M_vP_v}{M_{dry-air}(P-P_v)}, \tag{23}$$

where M_v=18 kg/kmol, and at the inlet to the channel $M_{ry-air}=\sum Y_iM_i\approx 29\,kg/kmol$. For the saturated air flow entering the channel (i.e. the relative humidity ϕ=100%), P_v=P_{sat} at the cell operating temperature, Eqn. 23 reduces to:

$$\frac{\dot{m}_v}{(\dot{m}_{in})_{dry}}=0.622\frac{P_{sat}}{P-P_{sat}}, \tag{24}$$

where the air-side channel pressure *P* is taken =5 atm in the present study. Replacing $\dot{m}_v$ from Eqn. 23 into Eqn. 22, one can obtain:

$$\dot{m}_{in}=(\dot{m}_{in})_{dry}\left[1+0.622\frac{P_{sat}}{P-P_{sat}}\right] \tag{25}$$

With the $(\dot{m}_{in})_{dry}$ known from Eqn. 21, $\dot{m}_{in}$ can be obtained using Eqn. 25. Finally, the u_{in} is obtained knowing the inlet area and density via: $u_{in}=\dot{m}_{in}A_{cl}/\rho_{in}A_{in}$. At inlet, all species mole fractions can be calculated from below relations:

$$Y_{H_2O}=\frac{P_{sat}}{P},\frac{Y_{O_2}}{Y_{N_2}}=\frac{21}{79},Y_{O_2}+Y_{N_2}=1 \tag{26}$$

Species mass fractions can be obtained as follows,

$$C_{g\,in}^{O_2}=\frac{Y_{O_2}M_{O_2}}{M_g},C_{g\,in}^{H_2O}=\frac{Y_{H_2O}M_{H_2O}}{M_g}, \tag{27}$$

where

$$M_g=Y_{O_2}M_{O_2}+Y_{N_2}M_{N_2}+Y_{H_2O}M_{H_2O}. \tag{28}$$

At boundary location *II*, fully developed conditions were used:

$$\frac{\partial u}{\partial x}=0,\frac{\partial v}{\partial x}=0,\frac{\partial C_g^{H_2O}}{\partial x}=0,\frac{\partial C_g^{O_2}}{\partial x}=0. \tag{29}$$

At boundary location *III*, wall boundary condition was applied, this boundary condition requires zero velocity and no mass transfer through it:

$$u = 0, v = 0, \frac{\partial C_g^{H_2O}}{\partial y} = 0, \frac{\partial C_g^{O_2}}{\partial y} = 0. \quad (30)$$

At boundary location *IV*, there are two other wall-type boundary conditions in porous GDL where:

$$u = 0, v = 0, \frac{\partial C_g^{H_2O}}{\partial x} = 0, \frac{\partial C_g^{O_2}}{\partial x} = 0, \frac{\partial s}{\partial x} = 0. \quad (31)$$

At boundary location *V* (the catalyst layer-GDL interface), oxygen is consumed and water is generated as the reaction product. It is assumed that there is a string of one cell depth at the GDL/catalyst layer interface, along which the conservation equations are applied. The mass flux of species O_2 and H_2O through the northern face of these cells can be related to the local current density via:

$$N_{O_2} = \frac{iM_{O_2}}{4F}, N_{H_2O} = \frac{iM_{H_2O}}{2F}, \quad (32)$$

where N_{O_2} and N_{H_2O} denote the mass fluxes of species O_2 and H_2O, respectively, and α is the net water transferred through the membrane taken equal to 0.3 in present study. For the formation of a water molecule two protons are required, and the coefficient 2 multiplied to α guarantees this matter. Moreover, the rate of transfer of protons through the membrane is proportional to the local current density i. So the mass flux of water through the membrane would be proportional with $2\alpha i$. Consequently, the mass fluxes of oxygen and water vapor through the northern faces of the cells (of the string) can be obtained from Eqns. 32.

The tangential velocity-component at this boundary is zero due to the no slip condition. Therefore, the advection mass fluxes through eastern and western faces of the cells for all of the species at this boundary will be zero. It is also noted that the nitrogen species acts as an inert component, i.e., not participating in the reaction. Hence, the vertical component of its mass flux is set to zero at this boundary.

Applying the mass conservation equation for the whole mixture (Eqn. 1) for the one cell depth string at the boundary location *V*, i.e., $\partial(\varepsilon\rho)/\partial t + \nabla.(\varepsilon \vec{N}) = 0$, and ignoring all of the flux components in horizontal direction (due to the no-slip condition), the discretized form of the equation at this boundary becomes:

$$\frac{\partial(\varepsilon\rho)}{\partial t}\Delta x \Delta y + \varepsilon(N)_{nf}\Delta x - \varepsilon(N)_{sf}\Delta x = 0, \quad (33)$$

where the subscripts nf and sf corresponds to the north and south faces, respectively. The mass fluxes $(N)_{nf}$ and $(N)_{sf}$ in Eqn. 33 are as follows:

$$(N)_{nf} = M_{O_2}\frac{i}{4F} - M_{H_2O}\frac{i}{2F}(1+2\alpha), (N)_{sf} = \rho v \quad (34)$$

where Δx and Δy are the horizontal and vertical dimensions of the cell, respectively. Equations 33 and 34 are solved for v, which can be used, in turn, as a boundary condition for the y-momentum throughout the main domain. Equations. 5 and 6 are used to obtain the disctrized form of the the mass conservation of the oxygen and water vapor at the boundary location (*V*). Similar to Eqn. 33 the horizontal components of the fluxes are set agian equal to zero. Therefore,

$$\frac{\partial(\varepsilon(1-s)\rho_g C_g^{H_2O})}{\partial t}\Delta x \Delta y + \varepsilon(N_{H_2O})_{nf}\Delta x - \varepsilon((1-s)N_{H_2O})_{sf}\Delta x = \dot{S}_g \Delta x \Delta y, \quad (35)$$

$$\frac{\partial(\varepsilon(1-s)\rho_g C_g^{O_2})}{\partial t}\Delta x \Delta y + \varepsilon(N_{O_2})_{nf}\Delta x - \varepsilon((1-s)N_{O_2})_{sf}\Delta x = 0, \quad (36)$$

where:

$$(N_{O_2})_{nf} = \frac{iM_{O_2}}{4F}, (N_{O_2})_{sf} = (\rho_{O_2} v_g + J_{O_2})_{sf}, \quad (37)$$

$$(N_{H_2O})_{nf} = -(1+2\alpha)\frac{iM_{H_2O}}{2F}, \quad (38)$$

$$(N_{H_2O})_{sf} = (\rho_{H_2O} v_g + J_{H_2O})_{sf}.$$

The diffusive mass fluxes J appeared in Eqns. 37 and 38 are calculated from the Maxwell-Stefan equation, Eqn. 7. Equations 33 and 34 are solved for $C_g^{H_2O}$ and $C_g^{O_2}$, which can be used in turn as the boundary conditions for Eqns. 5 and 6.

The Tafel equation is used to obtain the local current density distribution along the GDL/catalyst layer interface for a given

Overpotential [8],

$$i = i_0(1-s)\frac{C_g^{O_2}}{C_{g,ref}^{O_2}}\exp(\frac{\alpha_c F}{\bar{R}T}\eta), \quad (39)$$

where i_0 is the exchange current density and is the reference oxygen mass fraction, their ratio is taken as $i_0/C_{g,ref}^{O_2} = 0.03641 A/cm^2$ is the cathodic transfer coefficient, it is obtained using its relation with temperature ($\alpha_c = 0.5 + 2.3E-3(T-303)$) in the present study [11]. The coefficient (1-s) in Eqn. 39 is a correction factor accounting the reduced available surface (due to the saturation) for the electron delivery to the reaction sites.

5. RESULTS AND DISCUSSION

The cell potential (U) is calculated from $U = U_0 - \eta$, where U_0 is the reversible voltage given in [2]. The results obtained from the present computations at a sample overpotential η=0.735 V (i.e. at the cell voltage $\approx 0.935 - 0.735 = 0.2V$) are brought below. The comparison between numerical current density (1.86 A/cm^2) and experimental [2] current density (1.8405 A/cm^2) shows a good agreement.

Figure 3 shows the contours of the gas phase density ρ_g within the computational domain. The gas phase density decreases from the lower left corner where oxygen mass fraction (at the entrance) is higher than that at the upper right corner where it has been consumed in the favor of water production. Since the molecular weight of water vapor M_{H_2O} is less than that of the oxygen M_{O_2}, the resulting gas molecular weight M_g is higher at the lower left corner. Therefore, with the gas phase density obtained from $P/(R_g T) = PM_g/(\bar{R}T)$, ρ_g is much higher at the entrance (lower end corner) due to the enhanced M_g at this corner.

Figure 4 shows the contours of the oxygen mass fraction $C_g^{O_2}$ within the computational domain. Oxygen mass fraction decreases along channel especially adjacent to the catalyst layer where reaction exists and oxygen is consumed. Since the current density is directly related to oxygen mole fraction distribution at catalyst layer-GDL interface Eqn 39, the current density distribution trend Fig. 5 is similar to that of oxygen mass fraction Fig. 6 along the boundary V of Fig. 1. In Two-phase isothermal model, there is slightly difference between their trends. This difference is that the local current density profile is steeper than that of oxygen mass fraction at boundary V of Fig. 1. This is due to the effect of saturation (the coefficient (1-s) that is less than one) on local current density distribution Eqn. 39.

Figure 7 shows the contours of the water vapor mass fraction $C_g^{H_2O}$ within the computational domain. Water vapor mass fraction increases along catalyst layer. It has an inverse mass fraction trend in comparison with that of oxygen because the product of the oxygen-consuming reaction is water. (see Fig. 4 for comparisons).

Figure 8 shows the contours of the saturation s within the computational domain. Saturation is the result of water vapor condensation when water vapor partial pressure exceeds the saturation pressure at the mixture temperature. Water vapor partial pressure increases along the catalyst layer because of its mass fraction increment along the catalyst layer (see Fig. 7). That is why the saturation gets larger values from left to right Fig. 16).

Figure 10 shows the liquid flow field, as it is expected, the liquid is moving out of the GDL into the channel, there, it may drop down and is thrusted by shear force of gas velocity towards the gas channel outlet. It is noted that the x-component liquid velocity is very small in comparison with y-component liquid velocity

Figs. 13 and 15, so, the velocity vectors are normal to the flow stream.

Figure 11 shows the mass fraction distribution of nitrogen. It was expected that nitrogen mass fraction decreases along the channel. This is because two water molecules are produced per one oxygen molecule destruction along the channel that lessens the nitrogen presence with respect to the fact that the sum of all species mole fraction is one.

Figure 12 shows the two-phase mixture velocity field. There is a large difference in velocity magnitude between open channel and porous GDL. It seems that diffusion mass transfer mechanism becomes significant in GDL because the advection resulting from the bulk velocity is small.

The velocity in open channel must increase along the channel as Fig. 9 shows, this increase is due to mass injection into the channel from open channel-GDL interface.

Figure 13 shows the x-component liquid velocity profiles at three separate locations. The model shows that the x-component liquid velocity is negative almost anywhere and positive near GDL-open channel interface. The mixture velocity in GDL is very small, negative liquid velocity indicates that the liquid phase diffusive momentum is greater than mixture velocity momentum in magnitude but in reverse direction. Liquid phase diffusive momentum is negative anywhere because the saturation increases along channel at any y, resulting $\partial s/\partial x$ to be a positive value. But $\partial P_c/\partial s$ is negative for any saturation values $(0 < s < 1)$, so, with respect to Eqn. 40 $\partial P_c/\partial x$ is negative anywhere, resulting in negative horizontal phase diffusive momentum Eqn. 11. u_l is not always negative for all cell operating conditions, For example Fig. 14 shows u_l profiles for an operating condition in which inlet velocity is 30 (cm/s), in which u_l is positive anywhere. The gradient of the capillary pressure is determined using:

$$\frac{\partial P_c}{\partial x} = \frac{\partial P_c}{\partial s}\frac{\partial s}{\partial x} \qquad (40)$$

But near GDL-open channel interface, there is a considerably very large shear force that thrusts the two-phase mixture in this region with larger mixture mass-averaged velocity magnitude than that near catalyst layer, so, Two-phase mixture momentum in x-direction becomes greater than j_l in magnitude resulting in positive u_l in this region.

Figure 15 shows the y-component liquid velocity profiles at three separate locations. The model shows that

the y-component liquid velocity becomes larger from $y=h_{GDL}$ to $y=h_{gc}$ because phase change is not limited at catalyst layer-GDL interface, but it occurs at inner location in GDL, It is similar to an injection into a flow that increases the velocity.

6. ACKNOWLEDGMENTS

Financial support from the Renewable Energy Organization of Iran (SANA) is gratefully acknowledged. Also the conversion of the text from Latex to MS-Word has been done by Hoda and Ahmadreza Kermani. Their kind contributions are highly appreciated.

7. REFERENCES

[1] Bird, R.B., Steward, W. and Lightfoot, E.N., 2002, ``Transport Phenomena'', Wiley, New York.

[2] Ticianelli, E. A., Derouin, C. R., Redondo, A. and Srinivasan S.,1988,``Methods to Advance Technology of Proton Exchange Membrane Fuel Cells'' J. of The Electrochem. Soc., 135, 2209.

[3] Bernardi, D.M., Verbrugge M.W., 1991, ``Mathematical model of a gas diffusion electrode bonded to a polymer electrolyte'', AIChE J., 37 1151–-1163.

[4] Bernardi, D.M., Verbrugge M.W., 1992, ``A mathematical model for the solid-polymer-electrode fuel cell'', J. of The Electrochem. Soc.,139 2477–-2491.

[5] Springer, F.E., Zawodzinski, T.A., Gottesfeld S., 1991,``Polymer electrolyte fuel cell model'', J. Electrochem. Soc., 138 2334–-2342.

[6] Nguyen, T.V., White, R.E.,1993 , ``A water and thermal management model for proton-exchange-membrane fuel cells'', J. Electrochem. Soc., 140 2178–-2186.

[7] Gurau, V., Liu, H.T., Kakac, S.,1998 , ``Two-dimensional model for proton exchange membrane fuel cells'', AIChE J., 44 2410–-2422.

[8] Wang, Z.H., Wang, C.Y., Chen, K.S., 2001, ``Two-phase flow and transport in the air cathode of PEM fuel cells'', J. Power Source, 94 40–-50.

[9] Natarajan, D. and Nguyen, T. V., 2001, ``A Two-Dimensional, Two-phase, Multicomponent, Transient Model for the Cathode of a Proton Exchange Fuel Cell Using Conventional Gas Distributors'', J. of The Electrochem. Soc., 148 (12) A1324--A1335

[10] You, L. and Liu, H., 2002, ``A two-phase flow and transport model for the cathode of PEM fuel cells'', Int. J. of Heat and Mass Transfer, 45 2277–-2287

[11] Parthasarathy, A., Srinivasan, S., Appleby, J. A. and Martin, C. R., 1992,``Temperature Dependence of the Electrode Kinetics of Oxygen Reduction at the Platinum/Na on Interface – A Microelectrode Investigation'', J. of The Electrochem. Soc., 139(9):2530–-2537.

[12] Nguyen, P. T. B.E.Sc., 2003, ``A Three-Dimensional Computational Model of PEM Fuel Cell with Serpentine Gas Channels'', University of Western Ontario.

[13] Nam, J. H.; Kaviany, M., 2003, ``Effective Diffusivity and Water-Saturation Distribution in Single- and Two-Layer PEMFC Diffusion Medium'', Int. J. Heat and Mass Transfer, 46, 4595--4611.

[14] Khakbaz Baboli, M., 2007, ``A Two-Dimensional Computational model of cathode electrode of PEM fuel cells'', M.Sc. Thesis, Department of Mechanical Engineering, Amirkabir University of Technology (Tehran polytechnic), Tehran, Iran.

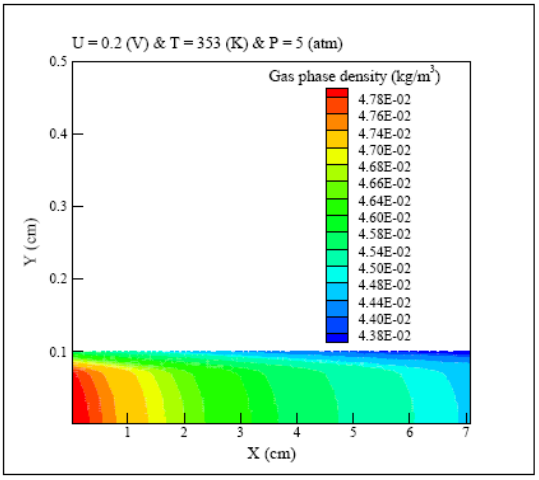

Figure 3. Gas phase density contours (kg/cm^3).

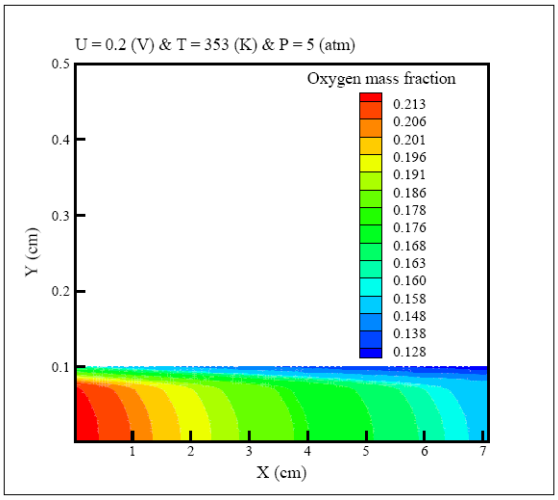

Figure 4. Oxygen mass fraction contours.

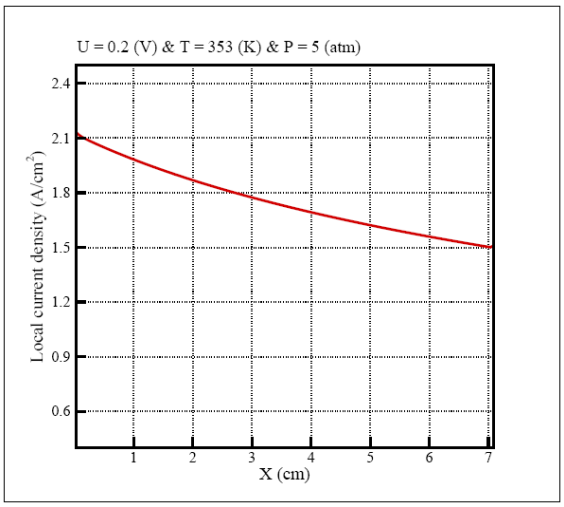

Figure 5. Local current density distribution along catalyst layer (A/cm^2).

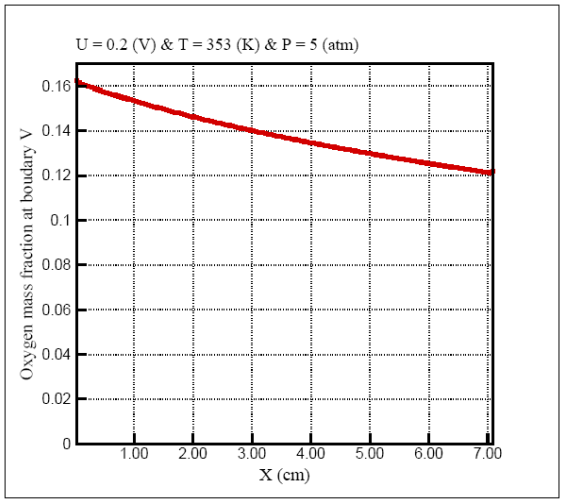

Figure 6. Oxygen mass fraction profile along boundary V of Fig. 1.

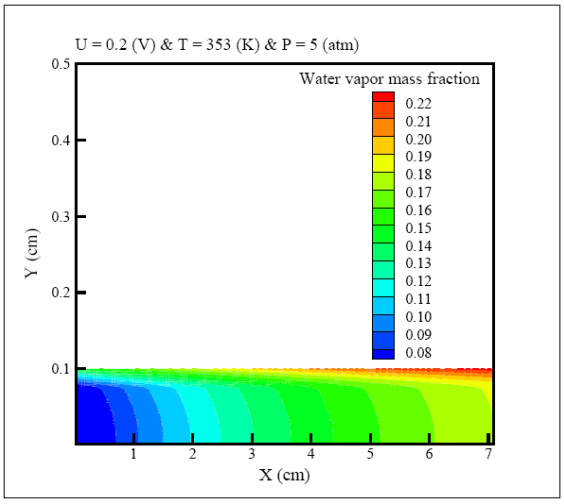

Figure 7. Water vapor mass fraction contours.

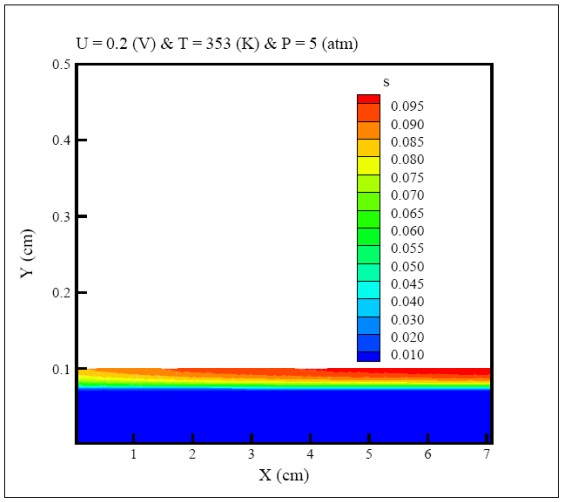

Figure 8. Saturation contours.

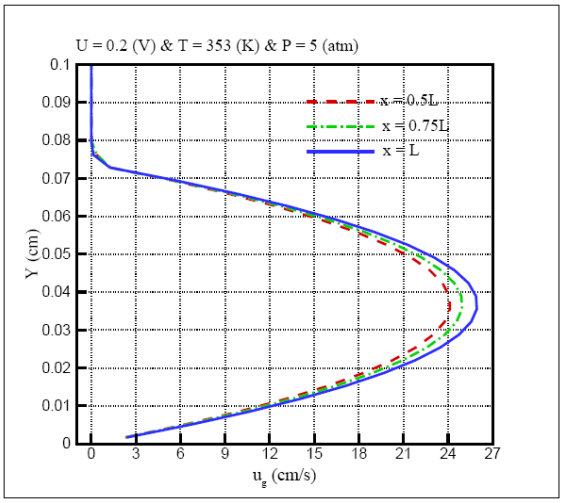

Figure 9. Comparative profiles of u_g (cm/s) at three stations $x = 0.5L$, $0.75L$ and L along the channel.

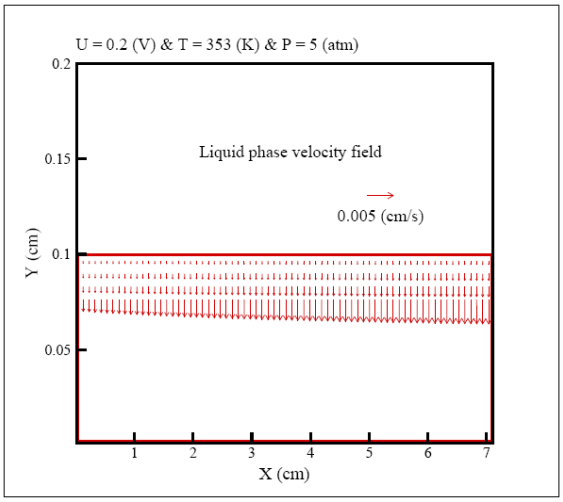

Figure 10. Liquid phase flow field (cm/s).

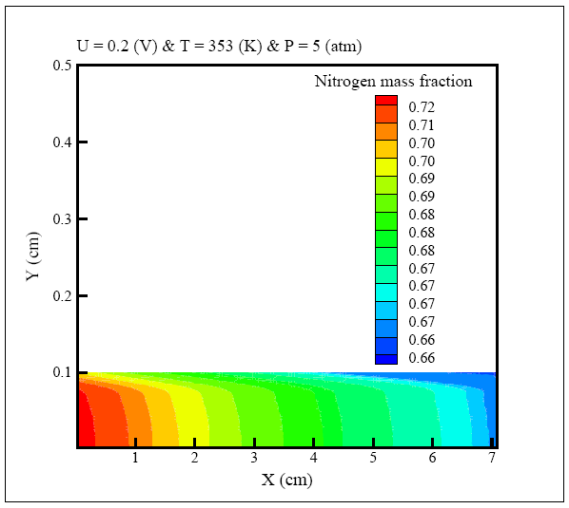

Figure 11. Nitrogen mass fraction contours.

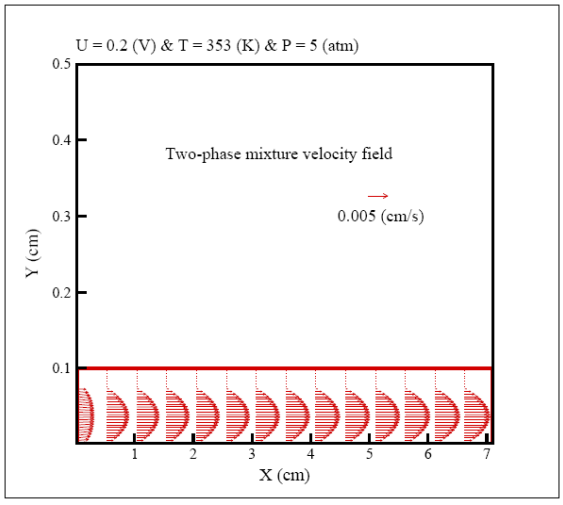

Figure 12. Two-phase mixture velocity flow field.

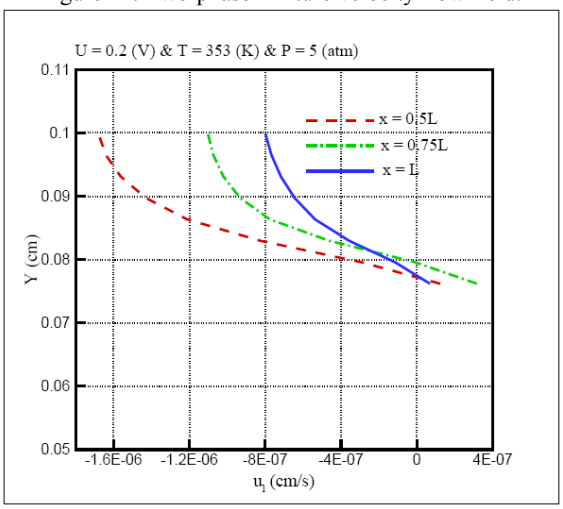

Figure 13. Comparative profiles of u_l (cm/s) at three stations $x = 0.5L$, $0.75L$ and L along the channel.

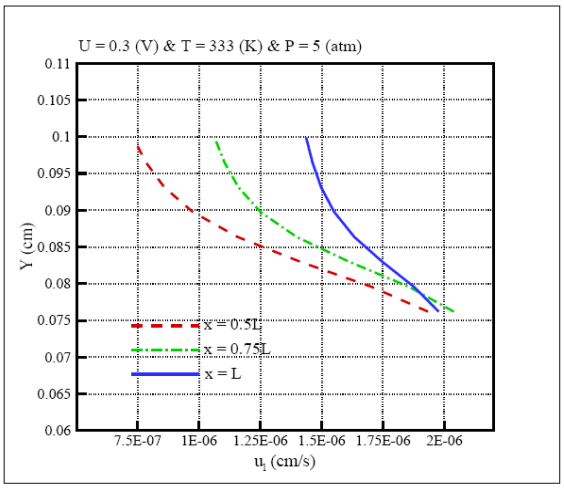

Figure 14. Comparative profiles of u_l (cm/s) at three stations $x = 0.5L$, $0.75L$ and L along the channel.

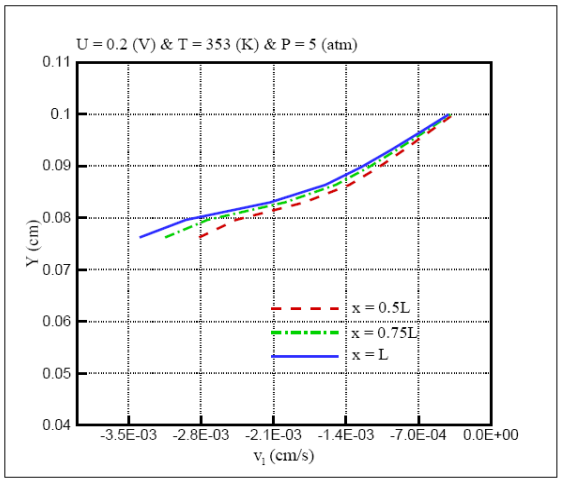

Figure 15. Comparative profiles of v_l (cm/s) at three stations $x = 0.5L$, $0.75L$ and L along the channel

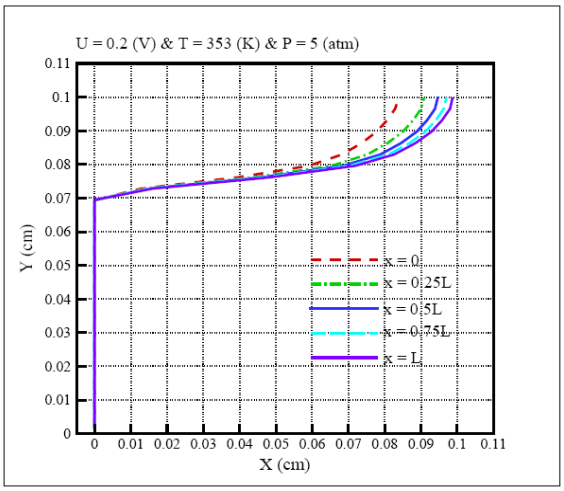

Figure 16. Comparative profiles of saturation (s) at five stations $x = 0$, $0.25L$, $0.5L$, $0.75L$ and L along the channel.